Study of the Impact of E-Machine in Hybrid Dual Clutch Transmission Powertrain

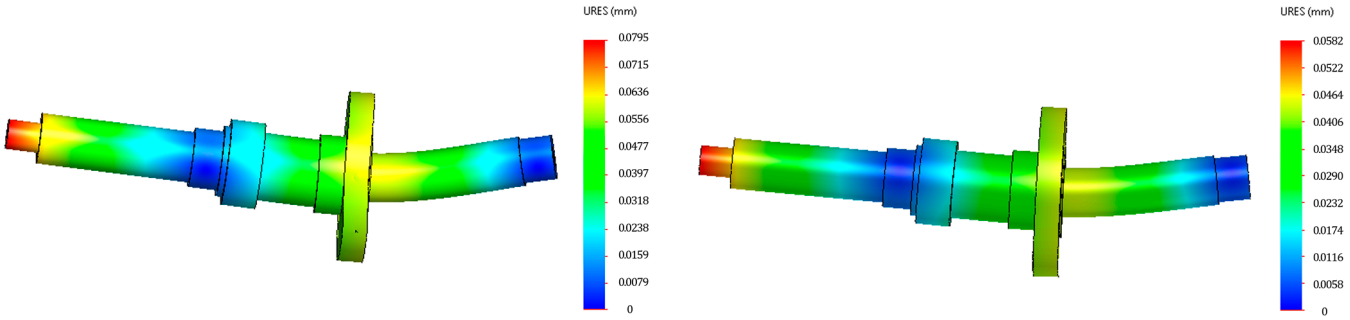

(**a**) (**b**)

Figure 8. Fourth gear results: (**a**) boost; (**b**) recuperation.

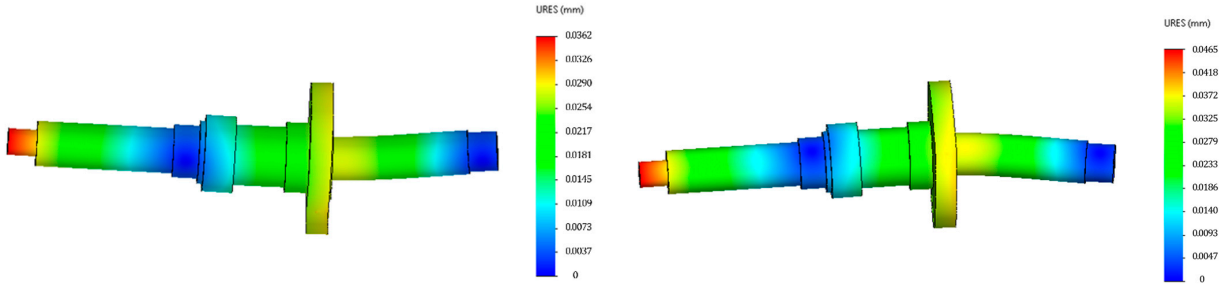

(**a**) (**b**)

Figure 9. Second gear results: (**a**) boost; (**b**) recuperation.

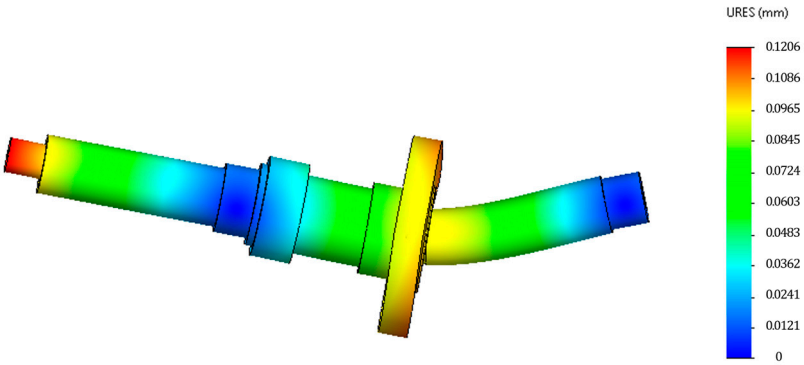

Figure 10. ICE + EM in 4th gear boost result.

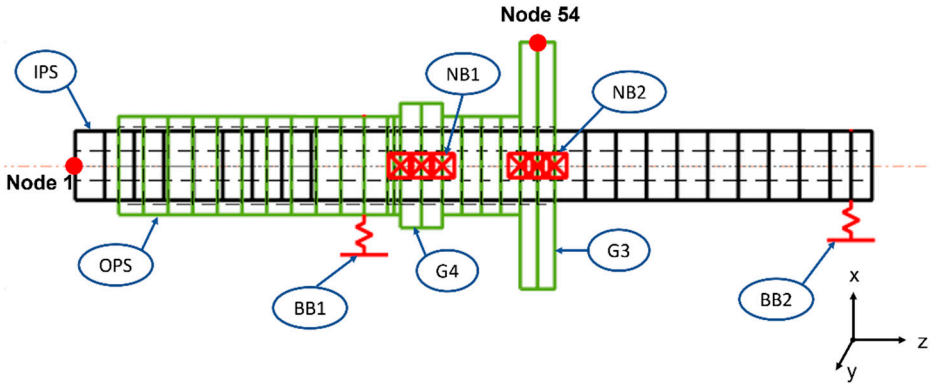

Figure 11. FEM model using DYNROT code for the dynamic analysis.

The rotating parts are assumed to be axially symmetrical so that linearized equation of motion for the undamped system in complex coordinate frame can be written as follows [38]:

$$[\boldsymbol{M}]\{\ddot{\boldsymbol{q}}\} - i\omega[\boldsymbol{G}]\{\dot{\boldsymbol{q}}\} + [\boldsymbol{K}]\{\boldsymbol{q}\} = \omega^2\{\boldsymbol{F}\}e^{i\omega t} \tag{18}$$

where, $\boldsymbol{M}$ is mass matrix, $\boldsymbol{G}$ is gyroscopic matrix, $\boldsymbol{K}$ is stiffness matrix, $\boldsymbol{F}$ is vector of unbalances, $\boldsymbol{q} = \left\{ \begin{array}{c} u \\ \psi \end{array} \right\}$ is vector of complex coordinates and ω is rotation speed.

The model includes 55 nodes in total with 2 complex degrees of freedom each, resulting in 110 degrees of freedom. The nodal displacements and rotations in complex coordinates involved in the flexural behavior are $u = u_x + iu_y$, $\psi = \psi_y - i\psi_x$ where u_x, u_y, ψ_x and ψ_y are the nodal displacements and rotations. The axial displacement u_z and the torsional rotation ψ_z are 2 additional real degrees of freedom that take the axial and torsional behavior into account, respectively. Each node has thus a total of 2 complex plus two real degrees of freedom. For this analysis only the flexural and torsional behavior are studied.

The model is used to determine the rotor Campbell diagram and critical speeds with the corresponding mode shapes. The effect of EM is evaluated considering two kind of dynamic effects:

1. Effect of EM inertia torque during shafts angular accelerations.
2. Effect of EM torque irregularities.

Both effects produce a torque that translates in contact forces acting on gears G1-G2-G3. Therefore, the problem has been studied by computing at varying speeds the transfer functions between the radial displacement at node 1 and the forces acting on node 54 as shown in Figure 11.

For transformation of the matrices from complex coordinates to real coordinates, the formulation in [33] has been used. Hence, the $q = \left\{ \begin{array}{c} u \\ \psi \end{array} \right\}$ in complex coordinates is changed to $q_{xy} = \left\{ \begin{array}{c} u_x \\ u_y \\ \psi_x \\ \psi_y \end{array} \right\}$ in real coordinates.

The equation of motion to study the flexural behavior in X-Y coordinates is written as in Equation (19). The description of variables is given in Table 3.

$$\boldsymbol{M_{xy}}\ddot{\boldsymbol{q}}_{\boldsymbol{xy}} + \left(\boldsymbol{L_{xy}} + \omega\boldsymbol{G_{xy}}\right)\dot{\boldsymbol{q}}_{\boldsymbol{xy}} + \left(\boldsymbol{K_{\omega oxy}} + \omega^2\boldsymbol{K_{\omega 2xy}} + \omega\boldsymbol{H_{xy}}\right)\boldsymbol{q_{xy}} \tag{19}$$

$$= \boldsymbol{f_{sxy}} + \omega^2\boldsymbol{f_{unb}}\left\{ \begin{array}{c} \sin(\omega t) \\ \cos(\omega t) \end{array} \right\} + \boldsymbol{S_{ixy}}\boldsymbol{f_{xy}}$$

Each node in real coordinates has four degrees of freedom compared to two degrees of freedom in complex coordinates. So, there are 220 degrees of freedom in total to describe the flexural behavior of the rotating system.

Dynamic Equation (19) can be reported, with explicit spin speed, in the state space representation in the following way, for X-Y behavior. The matrices are described in Table 4.

$$\dot{\boldsymbol{x}}(\boldsymbol{t}) = \left(\boldsymbol{A_{\omega 0}} + \omega\boldsymbol{A_{\omega 1}} + \omega^2\boldsymbol{A_{\omega 2}}\right)x(t) + \boldsymbol{Bu(t)} \tag{20}$$

$$\boldsymbol{y(t)} = \boldsymbol{Cx(t)} + \boldsymbol{Du(t)} \tag{21}$$

Table 3. Description of the variables.

Name	Description
ω	Spin Speed
q_{xy}	Generalized displacements
M_{xy}	Mass (symmetric) matrix
L_{xy}	Damping (symmetric) matrix
G_{xy}	Gyroscopic (skew-symmetric) matrix
$K_{\omega oxy}$	Stiffness (symmetric) matrix: spin speed independent
$K_{\omega 2xy}$	Stiffness (symmetric) matrix: spin speed dependent
H_{xy}	Circulatoric (skew-symmetric) matrix
f_{sxy}	Static forces
f_{unb}	Unbalance forces
f_{xy}	External forces
S_{ixy}	Input selection matrix
y	Output displacements
S_{oxy}	Output selection matrix

Table 4. Description of the matrices.

Name Description	Description
$x(t)$	$\begin{Bmatrix} q_{xy} \\ \dot{q}_{xy} \end{Bmatrix}$
$A_{\omega 0}$	$\begin{bmatrix} 0 & I \\ -M_{xy}^{-1}K_{\omega oxy} & -M_{xy}^{-1}L_{xy} \end{bmatrix}$
$A_{\omega 1}$	$\begin{bmatrix} 0 & 0 \\ -M_{xy}^{-1}H_{xy} & -M_{xy}^{-1}G_{xy} \end{bmatrix}$
$A_{\omega 2}$	$\begin{bmatrix} 0 & 0 \\ -M_{xy}^{-1}K_{\omega 2xy} & 0 \end{bmatrix}$
B	$\begin{bmatrix} 0 & 0 & 0 \\ I & I & S_{ixy} \end{bmatrix}$
$u(t)$	$\begin{Bmatrix} f_{sxy} \\ f_{unb} \\ f_{xy} \end{Bmatrix}$
$y(t)$	$\begin{Bmatrix} y_{xy} \\ \dot{y}_{xy} \end{Bmatrix}$
C	S_{oxy}
D	$[0]$
I	Identity Matrix

Finally, the transfer function between the displacement at node 1 and force at node 54 is computed from the state space that is used to calculate the displacement in the scenarios discussed later. The transfer function for different values of ω is depicted below in Figures 12 and 13. It can be seen that there are two peaks corresponding to the natural frequencies at 586 and 763 Hz. In Equation (19), it can be seen that the gyroscopic matrix (G_{xy}) is speed dependent and as a result the gyroscopic effect increases with the speed. Hence, in Figure 13, the absolute value of the transfer function increases with increase in speed.

The block shown in Figure 14 is used to calculate the displacement at the node 1, using the transfer function values shown in Figure 12. The inputs are ω, f_{xy} (forces generated due to ICE or EM torque irregularities which are described in the next subsection) and the frequency of the applied forces (2nd order harmonics for the ICE irregularities and 3rd order harmonics for the EM torque irregularities) and the output is displacement at node 1.

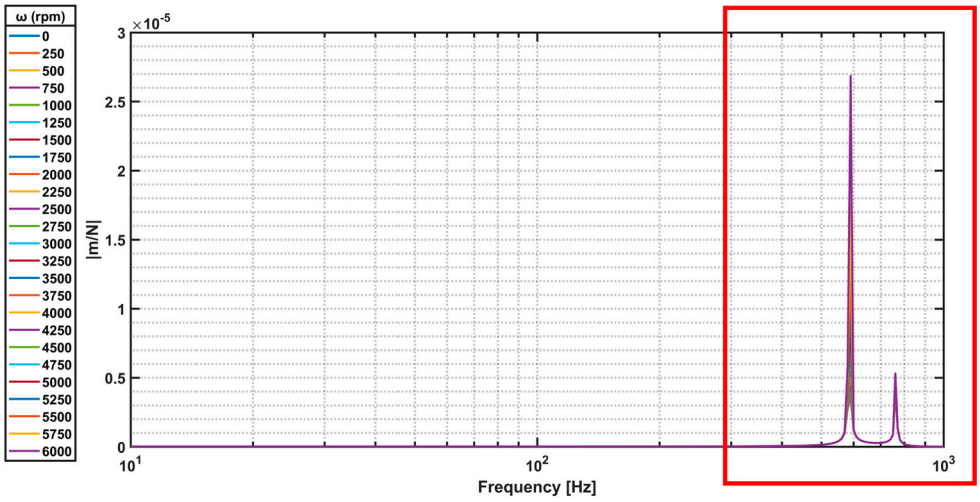

Figure 12. Transfer function plotted at different ω.

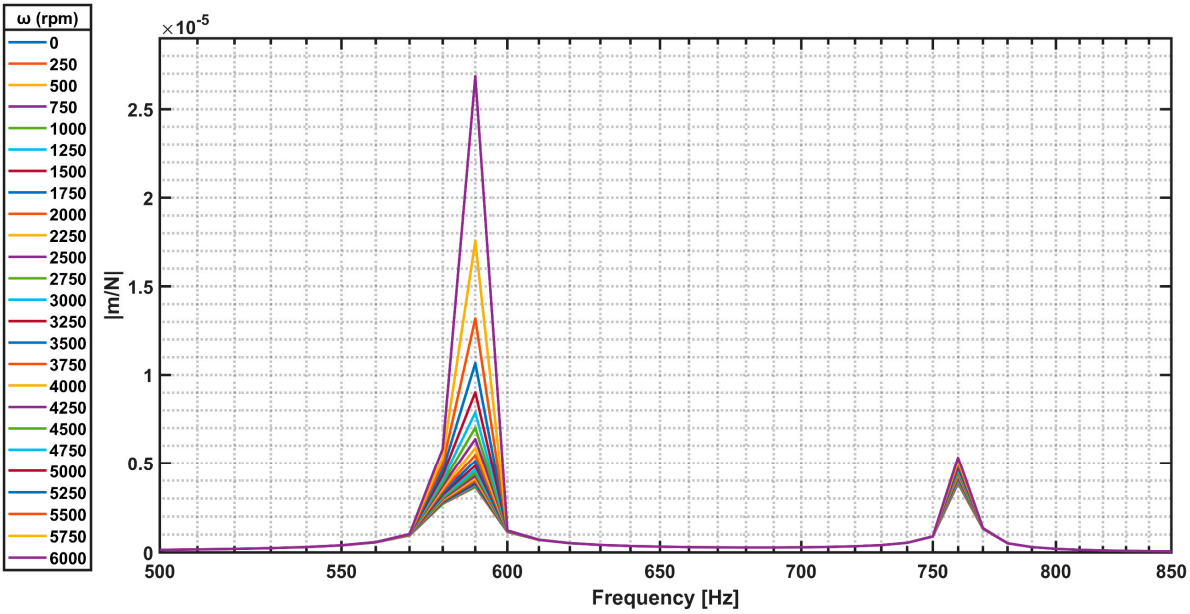

Figure 13. Transfer function plotted at different ω (zoom to the region of interest).

.

2.3.1. Scenario 1: Effect of EM Inertia Torque

Torque irregularities coming from the ICE (2nd order) plays a crucial role in the vibrations and deflections in the transmission. In this scenario, as depicted in Figure 15, the effect of the angular acceleration acting at the input of the transmission on the generation of the EM inertia torque are analyzed.

The speed of the *ICE* can be written as:

$$\omega_{ICE} = \omega_0 + \delta\omega \cdot \cos(2\omega_0 t) \tag{22}$$

where, ω_0 is the average *ICE* speed and $\delta\omega \cdot \cos(2\omega_0 t)$ represents the rotational speed irregularity that is present due to the 2nd order harmonics of the ICE.

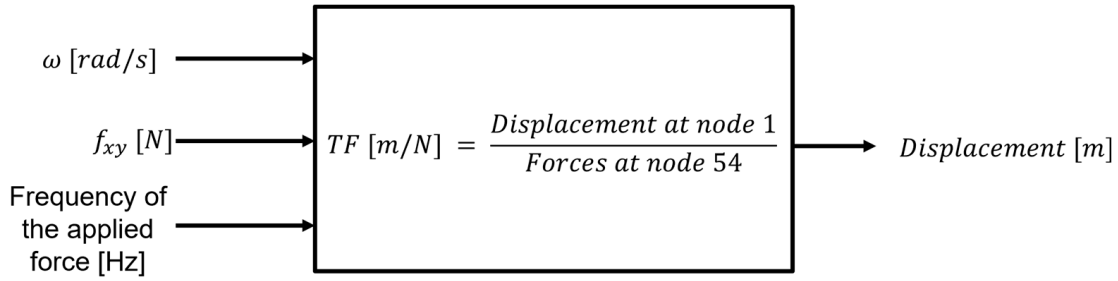

Figure 14. Transfer function block used to calculate the displacement.

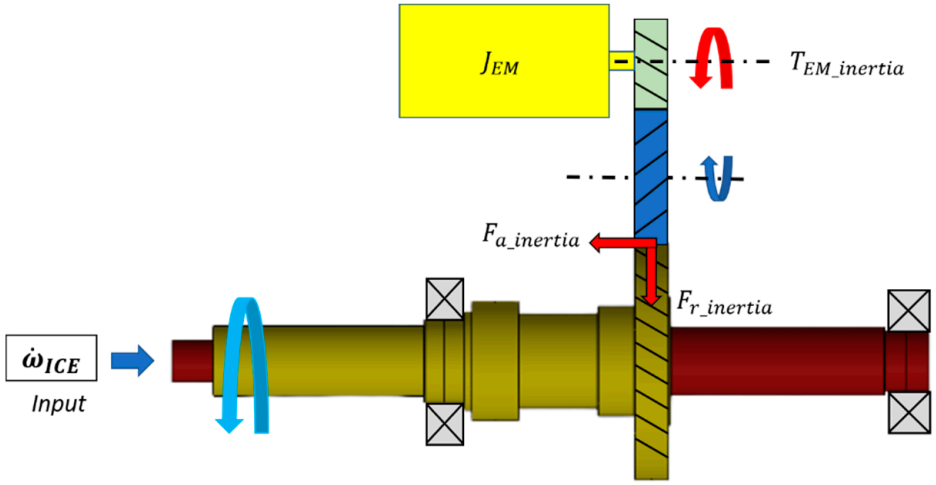

Figure 15. Setup for the EM inertia torque calculations.

The angular acceleration can be obtained by differentiating the Equation (22).

$$\dot{\omega}_{ICE} = 2\omega_0 \cdot \delta\omega \cdot \sin(2\omega_0 t) \tag{23}$$

The *EM* inertia torque is then calculated as follows:

$$T_{EM\ Inertia} = J_{EM}\ \dot{\omega}_{ICE}\ \tau_{G13} \tag{24}$$

where, J_{EM} is the inertia of the *EM*, $\dot{\omega}_{ICE}$ is the angular acceleration due to the torque irregularities and τ_{G13} is the gear ratio between primary shaft and EM.

Inertia torque $(T_{EM\_inertia})$ acts on gear G3 and generates tangential $(F_{t\_inertia})$, radial $(F_{r\_inertia})$ and axial $(F_{a\_inertia})$ forces with a frequency that corresponds to the 2nd order harmonics of the ICE, which produces the displacement at the front end of IPS.

2.3.2. Scenario 2: Effect of EM Torque Irregularities

Similar to ICE torque irregularities, the EM also have torque irregularities. The most important is represented by the 3rd order frequencies of the EM speed $(3\omega_{EM})$. EM torque irregularities $(T_{EM\_irregularities})$ generate tangential $\left(F_{t\_irregularities}\right)$, radial $(F_{r\_irregularities})$ and axial $(F_{a\_irregularities})$ forces that acts on the gear G3 as shown in Figure 16 and produce the displacements at the input of the inner primary shaft. In this scenario T_{EM} is considered as 1% of the total torque being transmitted by the EM, that is a function of the speed of the EM.

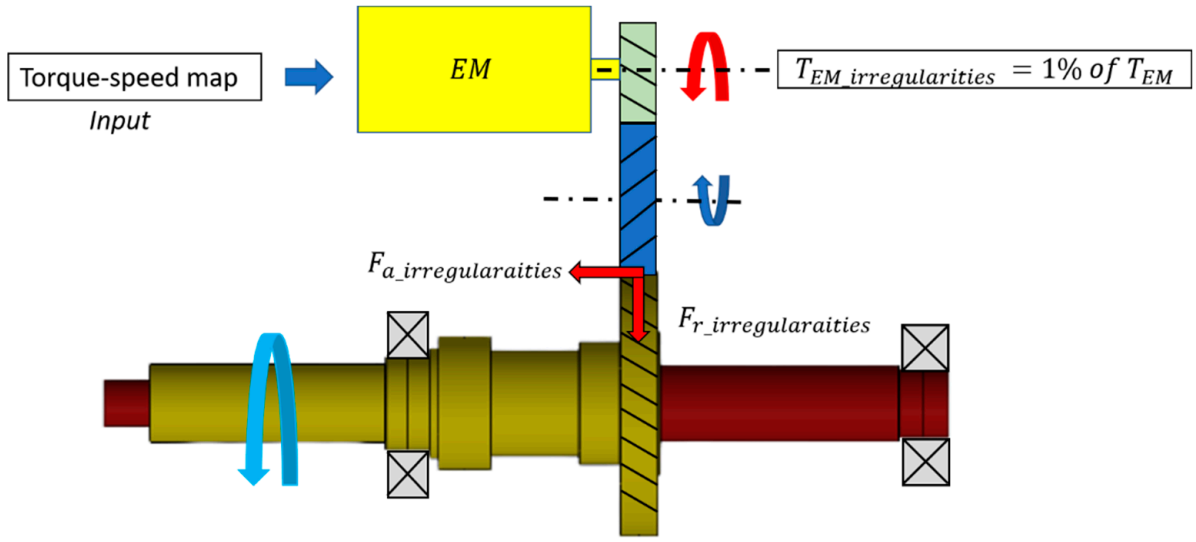

Figure 16. Description of the torque transmission path.

3. Results and Discussion

Rotor Dynamic Analysis Results

In this section, the results obtained from the rotor dynamic analysis carried out with DYNROT FEM code are presented and discussed. Campbell diagram for the model in Figure 11 is shown in the Figure 17. From the Campbell diagram it can be seen that there are two natural frequencies of the system at 586 and 763 Hz calculated at 0 rpm that can reach up to 590 and 764 Hz at 6000 rpm due to variation of the stiffness matrix ($\boldsymbol{K}_{\omega 2xy}$) in Equation (19) with speed. As far as the critical speeds are concerned, it can be seen that in the working range of the ICE from 800 to 6000 rpm, no critical speeds are present for synchronous speed. Moreover the 2nd and 4th order ICE harmonics do not show any critical speeds either. The only critical speed exists for the 3rd order harmonics of the EM, which is at 4700 rpm.

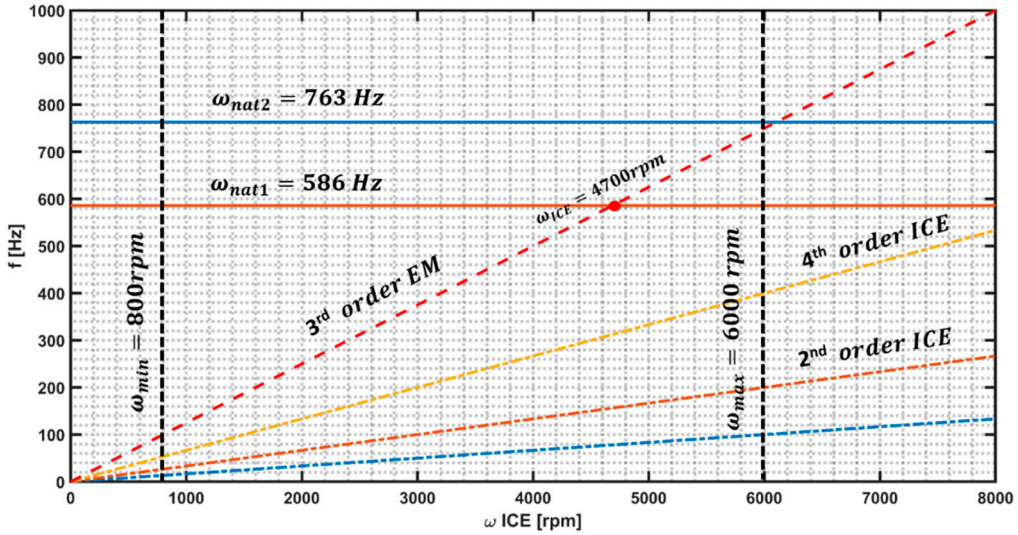

Figure 17. Campbell diagram.

The mode shape for the first critical speed is reported below in Figure 18. It can be seen that the IPS and OPS both have a deflection at the ends.

Figure 19 shows the displacement due to the EM inertia torque. It can be seen that the displacement increases as the ω increase. This can be attributed to the fact that the torque irregularities coming from the ICE increases with increase in the speed of ICE up to a certain rpm (2500 rpm). Above this speed the angular acceleration is considered constant and the increase in displacement at higher rpm is due to the high value of the transfer function that are dependent on speed.

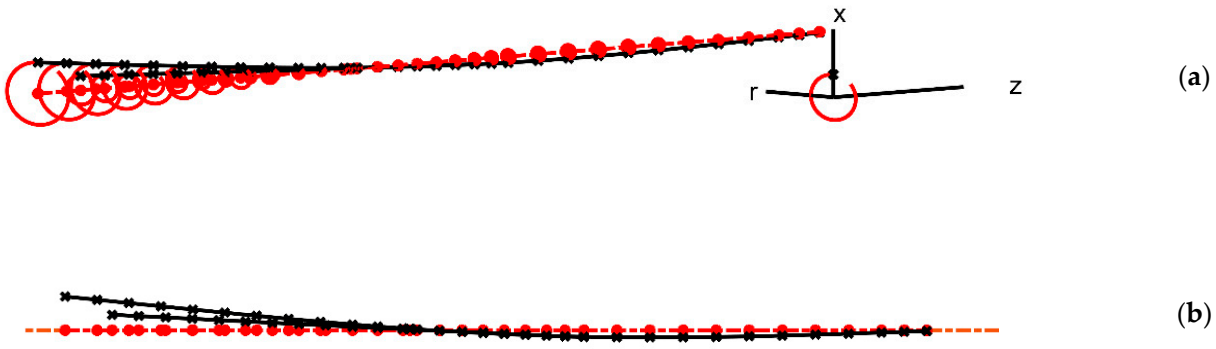

Figure 18. Mode shape: (**a**) 3D view; (**b**) 2D view.

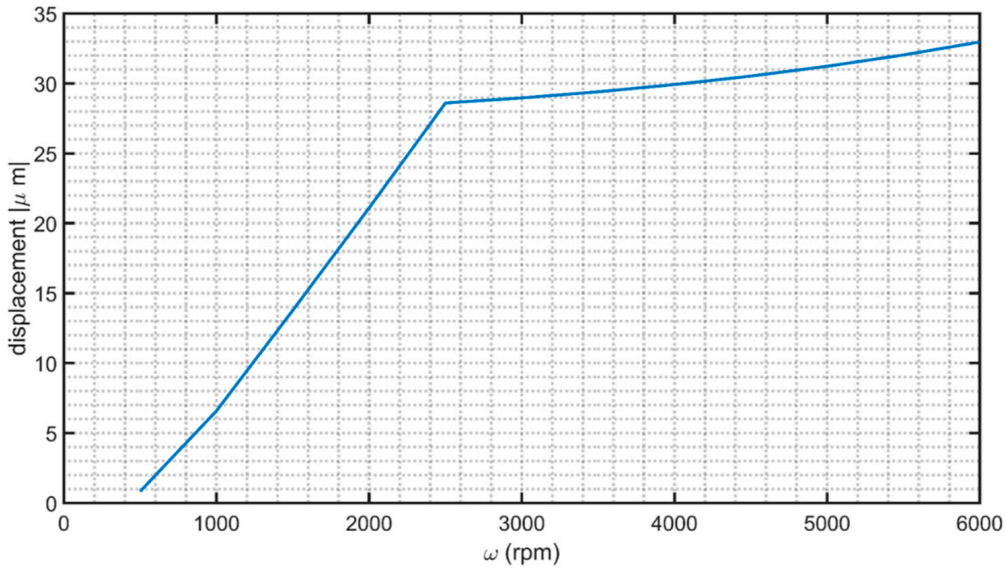

Figure 19. Displacement results for EM inertia torque.

Figure 20 shows the displacement due to the EM torque irregularities. It can be seen that the displacement reaches a maximum value of 92 µm at $\omega_{ICE} = 11750$ rpm. This is due to the fact that at this speed the 3rd order harmonics of the EM intersects with the first natural frequency as seen in the Campbell diagram (Figure 17).

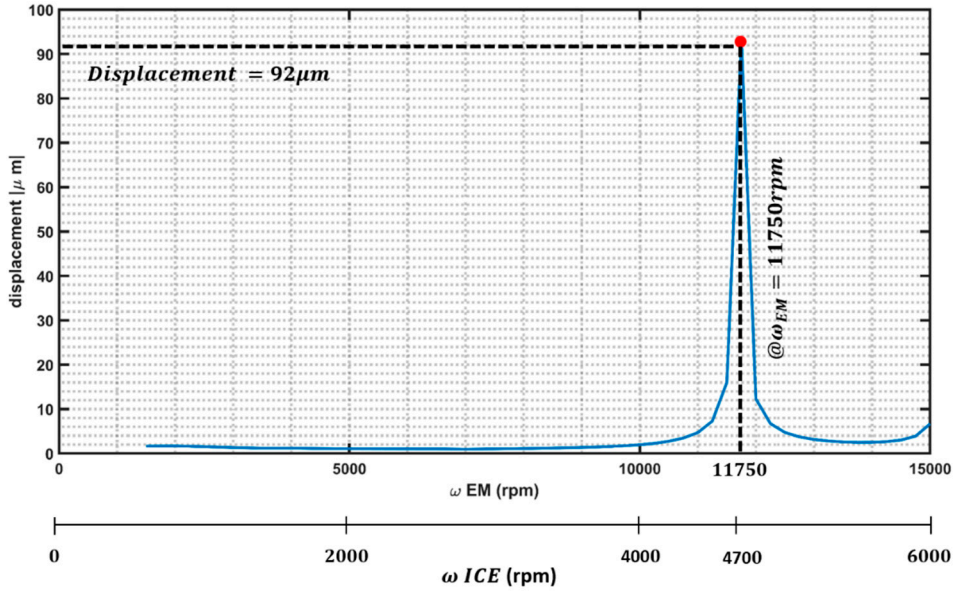

Figure 20. Displacement results for EM torque irregularities.

4. Conclusions

Multiple sources of excitation and frequently changing operating modes may introduce potential issues in terms of reliability for P2.5 hybrid powertrain with dual clutch transmission. The paper presents static and rotor dynamic analysis of the HDT in terms of radial displacements that arises at the DMF level due to additional torque transmission from the EM. The responsible of such radial displacement is the gear train transmission that links the EM to the primary shaft. The torque is transmitted by a tangential/radial/axial force causing bending on the primary shafts. Static analysis show that the maximum displacement of the shaft end can reach 120 μm in the case of torque transmission from both the power sources. On the other hand, rotor dynamic analysis shows that the displacements due to EM inertia torque are not high and can reach up to 33 μm at 6000 rpm, while they can reach up to 92 μm due to the EM torque irregularities. The combined static and dynamic effects can lead up to a maximum displacement of 242 μm, which is below the critical values (1.6 mm) indicated in service manual of the DMF manufactures [27]. However, this radial displacement can be amplified due to the manufacturing and assembling tolerances of the HDT and may reach close to the critical values of the radial gap in the DMF. Therefore, the manufacturing and assembling tolerances should be kept below the critical values of the DMF clearance, including the deflection coming from the EM torque transmission.

Author Contributions: Conceptualization, I.K., S.R., N.A. and A.T.; Data Curation, I.K.; Formal Analysis, I.K., S.R., N.A. and A.T.; Investigation, I.K., S.R. and N.A.; Methodology, N.A. and A.T.; Project Administration, N.A. and A.T.; Resources, I.K. and S.R.; Software, I.K.; Supervision, N.A. and A.T.; Validation, I.K. and A.T.; Visualization, I.K.; Writing—Original Draft, I.K. and S.R.; Writing—Review and Editing, I.K., S.R., N.A. and A.T. All authors have read and agreed to the published version of the manuscript.

Funding: This research received no external funding.

Institutional Review Board Statement: Not applicable.

Informed Consent Statement: Not applicable.

Data Availability Statement: Data is not available due to restrictions.

Acknowledgments: This work was developed in the framework of the activities of the Interdepartmental Center for Automotive Research and Sustainable Mobility (CARS) at Politecnico di Torino (www.cars.polito.it, accessed on 13 December 2021).

Conflicts of Interest: The authors declare no conflict of interest.

Appendix A

For this study, the DCT data used is from the 7-speed transmission from Magna (7DCT300) [39]. Gear ratios of the DCT used in this work are given below in the Table A1:

Table A1. 7DCT300 Gear ratios.

Transmission type:	Dual clutch
Number of gears:	7
Gear ratios (overall):	
I	4.462 (18.63)
II	2.824 (11.79)
III	1.805 (7.54)
IV	1.262 (5.27)
V	0.964 (4.03)
VI	0.771 (3.22)
VII	0.638 (2.66)
Final drive ratio:	4.176 (4.733 for 3rd and 5th gear)

Detailed CAD data regarding the DCT can be assessed from [40].

References

1. Regulation (EU) 2019/631 of the European Parliament and of the Council. Available online: https://eur-lex.europa.eu/legal-content/EN/TXT/PDF/?uri=CELEX:32019R0631&from=EN (accessed on 1 July 2021).
2. 2030 Climate Target Plan. Available online: https://ec.europa.eu/clima/policies/eu-climate-action/2030_ctp_en (accessed on 1 July 2021).
3. Shaheen, S.A.; Lipman, T.E. Reducing greenhouse emissions and fuel consumption. *IATSS Res.* **2007**, *31*, 6–20. [CrossRef]
4. Amati, N.; Tonoli, A.; Castellazzi, L.; Ruzimov, S. Design of electromechanical height adjustable suspension. *Proc. Inst. Mech. Eng. Part D J. Automob. Eng.* **2017**, *232*, 1253–1269. [CrossRef]
5. Ehsani, M.; Gao, Y.; Longo, S.; Ebrahimi, K.M. *Modern Electric Hybrid Electric and Fuel Cell Vehicles*, 3rd ed.; CRC Press: Boca Raton, FL, USA, 2018; Volume 82, p. 793.
6. Chen, H.; Li, L.; Küçükay, F. Study of series-parallel and power-split DHT for hybrid powertrains. *Automot. Innov.* **2021**, *4*, 23–33. [CrossRef]
7. Sieg, C.; Küçükay, F. Benchmarking of dedicated hybrid transmissions. *Vehicles* **2020**, *2*, 100–125. [CrossRef]
8. Rahmeh, H.; Bonfitto, A.; Ruzimov, S. Fuzzy Logic vs Equivalent Consumption Minimization Strategy for Energy Management in P2 Hybrid Electric Vehicles. In Proceedings of the 22nd International Conference on Advanced Vehicle Technologies (AVT), St. Louis, MO, USA, 17–19 August 2020; Volume 4.
9. Blessing, U.C.; Meissner, J.; Schweiher, M.; Hoffmeister, T. Scalable hybrid dual-clutch transmission. *Auto Tech. Rev.* **2015**, *4*, 46–51. [CrossRef]
10. Huang, W.; Zhang, J.; Huang, J.; Yin, C.; Wang, L. Optimal speed regulation control of the hybrid dual clutch transmission shift process. *World Electr. Veh. J.* **2020**, *11*, 11. [CrossRef]
11. Joshi, A.S.; Shah, N.P.; Mi, C. Modeling and simulation of a dual clutch hybrid vehicle powertrain. In Proceedings of the 2009 IEEE Vehicle Power and Propulsion Conference, Dearborn, MI, USA, 7–10 September 2009.
12. Walker, P.; Zhu, B.; Zhang, N. Powertrain dynamics and control of a two speed dual clutch transmission for electric vehicles. *Mech. Syst. Signal Processing* **2017**, *85*, 1–15. [CrossRef]
13. Liang, J.; Walker, P.D.; Ruan, J.; Yang, H.; Wu, J.; Zhang, N. Gearshift and brake distribution control for regenerative braking in electric vehicles with dual clutch transmission. *Mech. Mach. Theory* **2019**, *133*, 1–22. [CrossRef]
14. Mrochen, M.A.; Sawodny, O. Modeling and simulation of a hybrid dual-clutch transmission powertrain. *IFAC-PapersOnLine* **2018**, *51*, 886–891. [CrossRef]
15. Qin, Y.; Tang, X.; Jia, T.; Duan, Z.; Zhang, J.; Li, Y.; Zheng, L. Noise and vibration suppression in hybrid electric vehicles: State of the art and challenges. *Renew. Sustain. Energy Rev.* **2020**, *124*, 109782. [CrossRef]
16. Brandl, S.; Biermayer, W.; Graf, B.; Resch, T. Hybrid vehicle's NVH challenges and influences on the NVH development. *SAE Tech. Pap. Ser.* **2016**. [CrossRef]
17. Walker, P.D.; Zhang, N. Active damping of transient vibration in dual clutch transmission equipped powertrains: A comparison of conventional and hybrid electric vehicles. *Mech. Mach. Theory* **2014**, *77*, 1–12. [CrossRef]

18. Kim, S.; Choi, S.B. Cooperative control of drive motor and clutch for gear shift of hybrid electric vehicles with dual-clutch transmission. *IEEE/ASME Trans. Mechatron.* **2020**, *25*, 1578–1588. [CrossRef]
19. Sezer, V. Driving shaft lifetime enhancement by hybrid electrification. *Proc. Inst. Mech. Eng. Part D J. Automob. Eng.* **2018**, *233*, 572–584. [CrossRef]
20. Galvagno, E.; Vigliani, A.; Calenda, G. Dual-Mass flywheel with torque limiter: An effective solution for overtorque suppression in automotive transmission. *SAE Tech. Pap. Ser.* **2020**. [CrossRef]
21. Maffiodo, D.; Sesana, R.; Paolucci, D.; Bertaggia, S. Finite life fatigue design of spiral springs of dual-mass flywheels: Analytical estimation and experimental results. *Adv. Mech. Eng.* **2018**, *10*, 168781401877847. [CrossRef]
22. Laukenmann, M.A.; Sawodny, O. Model-Based control of a clutch actuator used in hybrid dual-clutch transmissions. *Mechatronics* **2021**, *77*, 102585. [CrossRef]
23. Mrochen, M.A.; Sawodny, O. Analysis and control of hybrid powertrains equipped with dual-clutch transmissions. In Proceedings of the 2020 American Control Conference (ACC), Denver, CO, USA, 1–3 July 2020.
24. Galvagno, E.; Velardocchia, M.; Vigliani, A. Torsional oscillations in automotive transmissions: Experimental analysis and modelling. *Shock Vib.* **2016**, *2016*, 5721960. [CrossRef]
25. Engine Bearing: Failure Analysis And Correction, Aftermarket, Mahle. Available online: https://www.mahle-aftermarket.com/media/local-media-north-america/pdfs-&-thumbnails/catalogs-and-literature/engine-bearings/ceb-2-1114-engine-bearing-failures-brochure.pdf (accessed on 12 December 2021).
26. Haneef, M.D.; Randall, R.B.; Peng, Z. Wear profile prediction of IC engine bearings by dynamic simulation. *Wear* **2016**, *364–365*, 84–102. [CrossRef]
27. Jang, J.Y.; Khonsari, M.M. On the wear of dynamically-loaded engine bearings with provision for misalignment and surface roughness. *Tribol. Int.* **2020**, *141*, 105919. [CrossRef]
28. Haneef, M.D.; Randall, R.B.; Smith, W.A.; Peng, Z. Vibration and wear prediction analysis of IC engine bearings by numerical simulation. *Wear* **2017**, *384–385*, 15–27. [CrossRef]
29. Naunheimer, H.; Bertsche, B.; Ryborz, J.; Novak, W. Design of gearwheel transmissions for vehicles. *Automot. Transm.* **2010**, 237–277.
30. Galvagno, E.; Guercioni, G.; Vigliani, A. Sensitivity analysis of the design parameters of a dual-clutch transmission focused on NVH performance. *SAE Tech. Pap.* **2016**. [CrossRef]
31. LuK Common Dual Mass Flywheel Issues. Available online: https://www.techtips.ie/LuK/common-dual-mass-flywheel-issues.pdf (accessed on 12 December 2021).
32. Taplak, H.; Parlak, M. Evaluation of gas turbine rotor dynamic analysis using the finite element method. *Measurement* **2012**, *45*, 1089–1097. [CrossRef]
33. Wilcock, D.F.; Booser, E.R. *Bearing Design and Application*; McGraw-Hill Company, Inc.: New York, NY, USA, 1957.
34. El-Sayed, H.R. Stiffness of deep-groove ball bearings. *Wear* **1980**, *63*, 89–94. [CrossRef]
35. Technical Report—NSK. Available online: http://www.nsk-literature.com/en/technical-report/offline/download.pdf (accessed on 12 December 2021).
36. Maitra, G.M. *Handbook of Gear Design*; Tata McGraw-Hill Education: New York, NY, USA, 1994.
37. Genta, G.; Delprete, C.; Bassani, D. DYNROT: A finite element code for rotordynamic analysis based on complex co-ordinates. *Eng. Comput.* **1996**, *13*, 86–109. [CrossRef]
38. Genta, G. *Vibration of Structures and Machines: Practical Aspects*; Springer Science & Business Media: Berlin, Germany, 2012.
39. Automobile Catalog: The Complete Catalog of Cars Since 1945. Available online: https://www.automobile-catalog.com/auta_details1.php (accessed on 12 December 2021).
40. DeVincent, E. Getrag DCT new modular platform from 100 Nm to 500 Nm. In Proceedings of the 7th International CTI Symposium, Detroit, MI, USA, 13–15 May 2013.